Unsteady vortex shedding dynamics behind a circular cylinder in very shallow free-surface flows

Fawaz Alzabari [a,b], Catherine A.M.E. Wilson [a], Pablo Ouro [a,c,*]

[a] Hydro-Environmental Research Center, School of Engineering, Cardiff University, Cardiff, CF24 3AA, Wales, UK
[b] Civil Engineering Department, College of Engineering, Najran University, Najran, 55461, Saudi Arabia
[c] School of Mechanical, Aerospace and Civil Engineering, University of Manchester, Manchester, M13 9PL, UK

ARTICLE INFO

ABSTRACT

The turbulent wake generated by a horizontal circular cylinder in free-surface flows of increasing shallowness with submergence-to-diameter ratios between 0.5 and 2.1 are investigated using large-eddy simulation. At Froude number (Fr) = 0.26, the free-surface deformation is small with little influence on the wake, whereas at $Fr = 0.53$ there is a drop in the free-surface downstream of the cylinder that impacts the coherence of the vortex shedding. Irrespective to the relative submergence, the close location of the cylinder to the bottom wall generates an asymmetric von-Kármán vortex street. Proper Orthogonal Decomposition (POD) is used to analyse the spatio-temporal coherence of the turbulent structures shed in the cylinder wake. The spatial patterns of the first two POD modes, those containing the most energy, depict the von-Kármán vortices. As Fr increases, the energy content of the first pair of POD modes decreases from 56% at $Fr = 0.26$ to 26.8% at $Fr = 0.53$, as large-scale vortices lose coherence more rapidly with shallower conditions. This energy redistribution leads to the smaller flow structures to contain a relatively higher energy when Fr is larger. The frequency of the dominating vortex shedding determined from the spectra of the POD temporal coefficients unveils that the first two coefficients feature a dominant peak at the von-Kármán vortex shedding frequency. At $Fr < 0.45$, the reconstructed flow field using the first 20 POD modes agrees well with the instantaneous velocities from LES, whereas free-surface effects on the wake dynamics at increasing Fr requires more POD modes to reconstruct the flow field with reduced error.

1. Introduction

The flow around a circular cylinder has been a classical and well-studied fundamental problem in fluid mechanics, which has been of interest to various areas of engineering and fundamental research due to its practical applications, such as offshore structures, pipelines or hydraulic structures. Recently in applications in more complex environments and cylinder arrangements relate the construction of woody debris dams for natural flood management [1], whose goal is to alleviate flood peaks. Problems with flow-induced vibration are prevalent in many of these engineering applications due to the periodic shedding of Kármán vortices [2,3]. In the construction and maintenance of sub-sea cables is critical to avoid any large vibration that can lead to a structural failure or even to long-term fatigue issues. Pipelines placed on erodible beds can induce a change in the flow dynamics that eventually causes sediment erosion that eventually leads to scour underneath the pipe, causing the pipeline to become a free-spanning structure likely to suffer from flow-induced loadings [4]. The understanding of the effects of cylinders in the surrounding environment remains a key topic.

Recent studies in the flow around circular cylinder cylinders have extended to incorporate the impact of asymmetric boundary conditions, i.e. near free or fixed surfaces [5]. The complex interaction of the cylinder wake and the distortion of the free surface leads to a more unsteady flow, altering the intrinsic properties and large-scale wake patterns associated with traditional isolated cylinder flows [6]. Whilst the flow past a circular cylinder in unbounded conditions has been extensively investigated for a wide range of Reynolds numbers [7,8], the modifications in the shear-layers and vortex shedding that can occur when the cylinder is positioned near a deformable free surface has received limited attention to date. In addition to the Reynolds number ($Re = U_0 D/\nu$, where U_0 the inflow velocity, D the cylinder diameter, and ν the kinematic viscosity of the fluid) that accounts for the turbulence regime; the effects of the free surface leads to the addition of three dimensionless parameters, namely the bulk Froude number ($Fr = U_0/\sqrt{gH}$ with g the gravitational acceleration and H the total water depth), the local Froude number ($Fr_h = U_t/\sqrt{gh}$ with h and U_t denote

---

the free-surface elevation overtopping the cylinder from its top side and velocity at this location, respectively), and the submergence ratio (h/D). The local Froude number is suitable to characterise the effect of the free-surface impact on the flow dynamics shortly downstream of the submerged cylinder [9].

Sheridan et al. [9] conducted one of the first experimental studies on cylinders near a free surface using Particle Image Velocimetry (PIV) for $Fr = 0.47$–0.72, $h/D = 0$–0.75 and $Re = 5{,}990$–$9{,}120$. They found that the unsteady interaction of the three separated high-vorticity regions from the free surface, and top and bottom ends of the cylinder, resulted in a jet-like flow with three different states including: attachment to the free surface, to the cylinder, and an intermediate state in between these. Reichl et al. [5] numerically investigated the flow past a single cylinder close to a free surface in laminar flow ($Re = 180$) over a wide range of submergence ratios from 0.1 to 5.0. For low Fr, the surface deformations were small, becoming more noticeable when Fr exceeded 0.3. They showed that the Fr_h was critical to account for free-surface undulations and wave breaking. At large Fr_h, the free-surface distortion is larger and leads to a diffusive flux of vorticity from the induced surface curvature, resulting in a substantially more asymmetric wake downstream of the cylinder. Kahraman et al. [10] studied instantaneous and time-averaged flow patterns around a horizontal circular cylinder in shallow flows at $Fr = 0.41$–0.71 and $Re = 1{,}124$–$3{,}374$ using PIV. Fr was found to be a driving parameter linked to the reattachment position to the free surface from the separated shear layers of the cylinder. Bouscasse et al. [11] used Smoothed Particle Hydrodynamic (SPH) to perform single-phase simulations that extended the range of global Fr up to 2.0 and provided an extensive flow taxonomy from the evaluation of the vorticity fields and free-surface distortions. They found a new wake state at $Fr \approx 1$, and the von-Kármán vortex shedding was observed to be recovered at high Froude numbers ($Fr \approx 2$). Further, Moballa et al. [12] observed the transition of the deformed free surface from regular waves to breaking waves, suggesting the close link between the hydrodynamic forces on the cylinder and submergence ratio. Zhao et al. [13] conducted large-eddy simulations for a submerged circular cylinder in a shallow channel flow for $Fr = 0.2$ and 0.6 based on the cylinder's diameter and $Re = 7{,}550$ to investigate the effects of the free surface distortion on the flow fields and hydrodynamics. While no obvious distortion of the free surface was found at $Fr = 0.2$, they classified the intense free-surface distortion occurring at $Fr = 0.6$ in three categories: a hydraulic jump in the overtopping region, wave generation region near the free surface, and a water level recovery further downstream.

Adequate quantification of how the unsteady turbulent wake dynamics changes requires the use of advanced techniques such as Proper Orthogonal Decomposition (POD) which is a reliable and explicit statistical methodology for identifying coherent patterns in transient flows. POD identifies the modes with the highest energy content and allows to represent the flow dynamics in a low-dimensional manner [14]. The use of reduced-order modelling via POD can provide new insights into the turbulent structures and also save computational time to enhance the efficiency of numerical models in fluid mechanics [15–17]. The adoption of POD to identify the largest scales of motion in cylinder flows has been successfully done in previous studies. For instance, Rehimi et al. [18] conducted an experimental study of the impact of wall confinement on the wake formation behind a circular cylinder at Re below 277 using PIV, and employed POD for a filtering purpose and to extract the energetic contribution of different modes. Sen et al. [19] conducted a numerical simulation of two-dimensional laminar flow past a circular cylinder at $Re = 100$ using a co-counter flow with various fluids to try to suppress vortex shedding by jet injection. They used POD to identify the dominant modes and their respective enstrophy distribution for the vorticity field. Wang et al. [20] investigated the near wake of a wall-mounted finite-length square cylinder applying POD to the PIV data, with the main focus on the correlation between flow structures and POD coefficients. Mishra and De [21] investigated the

suppression of vortex shedding using a passive flow control technique at $Re = 100$–500, and employed POD to quantify its effectiveness and also to investigate the dominant vortical structures.

To date most studies investigating free-surface cylinder flows considered mostly laminar flow regimes at low Reynolds numbers. Thus, the impact of free-surface proximity on the wake structures behind a cylinder in turbulent flow conditions has not been fully addressed, which is challenging as the vortical structures lose coherence faster at higher Reynolds number flows as viscosity forces diminish. The present study aims at evaluating the influence of free-surface effects on the wake downstream of a horizontal cylinder at $Re = 13{,}333$ with five submergence ratios ranging from $h/D = 2.1$ to 0.5 and resolved with Large-Eddy Simulation (LES). A detailed quantification of the developed wake dynamics is performed using POD, necessary to understand how the governing flow mechanisms vary with submergence depth.

The paper is structured as follows: the governing equations for LES are discussed in Section 2 together with the POD methodology. Section 3 presents the results including the instantaneous and the turbulent flow field obtained from LES at the different submergence depths considered, and then reports a detailed description of the flow structures based on their POD spatial modes, temporal coefficients, and energy distribution. The reconstructed velocity field using different numbers of POD modes is also discussed. Finally, the main findings of this study are discussed in Section 4.

2. Numerical framework

2.1. Computational model

The in-house code Hydro3D is used to perform large-eddy simulations [22], which is based on the finite differences method with a staggered storage of velocities in rectangular Cartesian grids and was shown to be computationally very efficient [23]. The code has been well validated in a series of challenging hydro-environmental engineering problems, such as tidal steam turbines [24], flow over bridge abutments [25], solitary waves [26], free-surface flow over square bars [27,28] and in pipes [29], or rough beds [30–32], among others. Hydro3D is based on the LES approach in which the energetic portion of the flow is explicitly resolved and the small-scale turbulence is modelled using a sub-grid scale model [33]. The Wall-Adapting Local Eddy-viscosity (WALE) sub-grid scale model from Nicoud and Ducros [34] is employed to compute the effects of the unresolved small-scale turbulence. Hydro3D solves the spatially-filtered Navier–Stokes equations for incompressible flow, that read:

$$\frac{\partial u_i}{\partial x_i} = 0 \tag{1}$$

$$\frac{\partial u_i}{\partial t} + \frac{\partial u_i u_j}{\partial x_j} = -\frac{1}{\rho}\frac{\partial p}{\partial x_i} + \nu \frac{\partial^2 u_i}{\partial x_j \partial x_j} - \frac{\partial \tau_{ij}}{\partial x_j} + f_i + F_{sf} + g_i \tag{2}$$

where u_i and u_j are the resolved velocity vectors (i or $j = 1, 2$, and 3 represent x-, y- and z-direction, respectively; and similarly, x_i, x_j represent the spatial location vectors in the three spatial directions; ρ is the density of the fluid, p is the resolved pressure, ν is the fluid kinematic viscosity, τ_{ij} is the subgrid-scale stresses, f_i represents external forces calculated using the direct forcing method proposed by Uhlmann [35] which is a diffused interface method that enforces a no-slip condition at the immersed boundary points comprising the geometry of the circular cylinder, F_{sf} is the surface tension force, and g_i is the gravitational acceleration. A fractional step method is employed to advance the simulation in time using a three-step low-storage Runge–Kutta scheme with a multi-grid method for the resolution of the Poisson's equation for pressure. The diffusive terms in the Navier–Stokes equations are approximated by second-order central differences, while convective velocity fluxes in the momentum conservation equation and the advection equation from the level-set method are approximated using a 5th-order weighted essentially non-oscillatory (WENO) scheme. The main

advantage of the WENO scheme is its capability to achieve the necessary compromise between numerical stability and physical accuracy when simulating two-phase flows [23]. Hydro3D is parallelised via a Message Passing Interface (MPI) and employs a domain decomposition technique to divide the computational domain into rectangular units that run on multiple CPUs.

The level set method (LSM) developed by Osher and Sethian [36] is adopted to resolve the free-surface between the air and water phases. The LSM employs a level-set signed distance function, ϕ, with values of $\phi > 0$ denoting water (liquid fraction) whilst $\phi < 0$ corresponds to the air (gas fraction) and has zero value at the air–water interface. The ϕ function is tracked over time by solving a pure advection equation in addition to the mass and momentum conservation equations:

$$\frac{\partial \phi}{\partial t} + u_i \frac{\partial \phi}{\partial x_i} = 0 \qquad (3)$$

Due to the inherent nature of the advection equation, the mass conservation is not ensured, as the required numerical stability criterion of $|\nabla \phi| = 1$ is not directly satisfied. Therefore, LSM is re-initialised to ensure that this stability criterion is accomplished at every time step, which is essential to maintain mass conservation in the computational domain [37].

A Heaviside function, $H(\phi)$, is employed at the air–water transition to allow a smooth transition and avoid numerical instabilities due to any sudden change in density (ρ) and viscosity (μ) between the two immiscible fluids [23,26]. The smoothed Heaviside function is defined as:

$$H(\phi) = \begin{cases} 0 & \text{if } \phi < -\varepsilon \\ \frac{1}{2} + \frac{1}{2}\left[\frac{\phi}{\varepsilon} + \frac{1}{\pi}\sin\left(\frac{\pi\phi}{\varepsilon}\right)\right] & \text{if } |\phi| \leqslant \varepsilon \\ 1 & \text{if } \phi > \varepsilon \end{cases} \qquad (4)$$

where ε is equal to $2.0 \cdot \Delta x_i$, and as defined in Kang and Sotiropoulos [38] it is an adjustable parameter that sets the thickness of the numerical smearing at the interface. Finally, the density and dynamic viscosity fields are calculated as:

$$\rho(\phi) = \rho_a + (\rho_w - \rho_a) H(\phi)$$
$$\mu(\phi) = \mu_a + (\mu_w - \mu_a) H(\phi) \qquad (5)$$

where the subscripts w and a represent water and air, respectively. A Continuum Surface Force (CSF) model [39] is implemented as a surface tension model, which is required to maintain the accuracy of the free-surface simulation when there is a significant surface breaking and air trapping the bulk of fluid forming small droplets and bubbles. The surface tension force F_{sf} is defined as follow:

$$F_{sf} = \sigma k \delta(\phi) n_i \qquad (6)$$

where σ is the coefficient of the surface tension equal to 0.728, k is the curvature of the interface and n_i is the unit vector normal to the liquid interface, which are computed as:

$$k = -\nabla n_i \qquad (7)$$
$$n_i = \frac{\nabla \phi}{|\nabla \phi|} \qquad (8)$$

The smoothed delta function, $\delta(\phi)$, in Eq. (6) corresponds to the spatial derivative of the Heaviside function in Eq. (4) and reads:

$$\delta(\phi) = \begin{cases} \frac{1}{2}\left(1 + \cos\frac{\pi\phi}{\varepsilon}\right), & \text{if } |\phi| < \varepsilon \\ 0, & \text{otherwise} \end{cases} \qquad (9)$$

2.2. Computational setup

The experimental setup of the horizontal circular cylinder in an open-channel flow presented in Muhawenimana et al. [40] is adopted. The cylinder has a diameter (D) equal to 0.05 m and is located at a vertical gap (G) of 0.025 m measured from the lower side of the

Table 1
Details of the cases studied including mean water depth (H), submergence depth (h), submergence ratio (h/D), Froude number (Fr) and local Froude number (Fr_h).

H [m]	h [m]	h/D [-]	Fr [-]	Fr_h [-]
0.18	0.105	2.1	0.26	0.36
0.15	0.075	1.5	0.31	0.46
0.12	0.045	0.9	0.40	0.59
0.11	0.035	0.7	0.45	0.73
0.10	0.025	0.5	0.53	0.89

cylinder and bottom wall, which corresponds to a gap ratio (G/D) of 0.5. The computational domain presented in Fig. 1 measures 1.5 m, 0.24 m and 0.01 m in the streamwise (x), vertical (z) and spanwise (y) directions, respectively. The origin of the x coordinates is chosen as the downstream end of a horizontal cylinder, which is placed $10.5D$ from the upstream inlet. The grid is uniform in the whole domain with a resolution of $\Delta x/D = \Delta z/D = 0.01$ in x and z direction respectively, while it is doubled in the spanwise direction. Therefore, the whole numerical mesh consists of 14.4 million grid cells, namely, $N_x \times N_y \times N_z = 3000 \times 10 \times 480$, where N_{x_i} indicates the number of grid nodes for each spatial direction.

The bulk velocity (U_0) is equal to 0.2667 m/s, resulting in a Reynolds number ($Re = U_0 D/\nu$) equal to 13,333. In order to investigate the free-surface effect on the wake structure of the cylinder, the mean water depth (H) is varied, resulting in different submergence depths (h), calculated from the upper side of the cylinder to the free-surface elevation obtained a posteriori in the simulation (see Fig. 1). The submergence depth varies with the adopted water depth in the range of $h = 0.025$–0.105 m, resulting in Froude numbers ($Fr = U_0/\sqrt{gh}$) ranging from 0.26 to 0.53. Table 1 provides details of the water depth, submergence ratio, Froude number, and local Froude number for the five cases proposed.

In the current LES, a mean logarithmic velocity profile is prescribed at the domain inlet according to a smooth log-law distribution with friction velocity (u_*) equal to 0.033 m/s obtained from the experimental velocity measurements [40], which is defined as:

$$\frac{u(z)}{u_*} = \frac{1}{\kappa} \ln\left(\frac{z u_*}{\upsilon}\right) \qquad (10)$$

Here $\kappa = 0.41$ is the von-Kármán constant. A convective boundary condition is used at the outflow. A no-slip boundary condition is imposed at the bottom boundary and periodic boundary conditions are used in the spanwise direction. The water surface deformation is calculated by the level-set method and the top of the domain is treated with a slip condition. The time step is variable with a Courant–Friedrichs–Lewy (CFL) condition of 0.2 in order to maintain a stable simulation. All simulations are executed on 200 CPUs and averaging of the flow statistics begins after about four flow-through periods ($T_f = L_x/U_0$, where L_x is the length of the domain) after the initial flow transients have vanished and then continued for about 30–40 flow-through periods to compute mean flow statistics once the flow is fully develop. The simulations are then restarted to generate transverse planes at equal time intervals between successive snapshots. Numerical results from the LES were validated in a previous LES study in Ouro et al. [6] using a rigid-lid (RL) approach that represented an undeformed air–water interface at $Fr = 0.31$ in comparison to the laboratory experiments from Muhawenimana et al. [40].

2.3. Proper orthogonal decomposition

Proper orthogonal decomposition (POD), also known as principal component analysis (PCA) or Karhunen–Loève decomposition, was first introduced in the context of turbulence by Lumley [41]. The POD method is a statistical methodology that can be used to study events that are expected to exhibit certain dominant recurrent patterns [42],
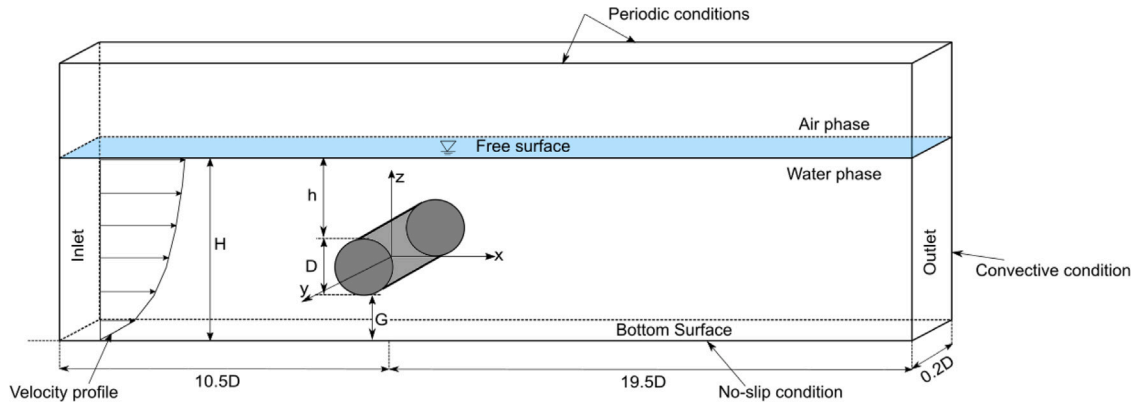
Fig. 1. Schematic of the computational domain adopted for the large-eddy simulation with the horizontal cylinder of diameter (D) located at a height G from the bottom surface. The total water depth is denoted by H whilst that free-surface elevation overtopping the cylinder is h. The inflow boundary condition with a logarithmic velocity distribution is also indicated.

with both the direct and snapshots methods have proven effective to obtain the dominant modes in turbulent flows [43]. Here, the snapshot POD method proposed by Sirovich [44] is used as it allows to reduce the number of data required during the POD procedure. The POD analysis is performed using the LES data obtained at xz-plane at the centre of the computational domain in the transverse y-direction (see Fig. 1). POD was initially applied to both streamwise and vertical velocities fluctuations obtained from the wake of the circular cylinder but the results obtained using the vertical velocity fluctuation (w') appeared more efficient for characterising the energetically dominant modes [45]. Therefore, only the latter one is used in the present POD analysis. The following is a brief description of the snapshot POD method and more details about the POD method can be found in [19,20].

A given spatio-temporal velocity field $w(x_i, t)$ can be decomposed into the mean velocity field and a fluctuating component, such that:

$$w(x_i, t) = \overline{W}(x_i) + w'(x_i, t) \tag{11}$$

where $\overline{W}(x_i)$ is the mean flow field, and $w'(x_i, t)$ is the fluctuating component. The values of the quantity w are obtained at M different spatial locations (x_i) for N temporal snapshots with equal time interval between them. The time-averaged velocity $\overline{W}$ is calculated and then subtracted from each of the instantaneous velocity w values to build the snapshot matrix W of order $M \times N$ from the resulting fluctuating velocity component, which reads:

$$W = \begin{bmatrix} w'(1,1) & w'(1,2) & \dots & w'(1,\ N) \\ w'(2,1) & w'(2,2) & \dots & w'(2,N) \\ \vdots & \vdots & \vdots & \vdots \\ \vdots & \vdots & \vdots & \vdots \\ w'(M,1) & w'(M,2) & \dots & w'(M,N) \end{bmatrix} \tag{12}$$

The autocovariance matrix C is calculated as $C = W^T W$. A set of N eigenvalues (λ^i) and associated eigenvectors (A^i) of the matrix C which satisfy $CA^i = \lambda^i A^i$ are evaluated. The eigenvalues are arranged in descending order, i.e. starting from the most energetic, and each denotes the mode's energy $(\lambda^1 > \lambda^2 > \cdots > \lambda^N > 0)$, with the sum of all eigenvalues reflecting the total energy. Alternatively, one can employ the singular value decomposition (SVD) of the matrix W [42]. In the present work, the SVD approach is employed to decompose the total snapshots into POD eigenmodes (up to 200 modes are selected here). The real $M \times N$ matrix W upon SVD is given by $W = U\Sigma V^T$ where U is an orthogonal matrix with range $M \times M$ whose columns are the eigenvectors of WW^T, V is an $N \times N$ orthogonal matrix whose columns are the eigenvectors of $W^T W$ (which is the autocovariance matrix C of the snapshot POD method). Σ is an $M \times N$ diagonal matrix with non-negative real numbers in the diagonal, which are called the singular values of the matrix W, whose entries are the square root

of the eigenvalues of $W^T W$ or C. The spatial eigenvectors of C are represented by the columns of V, whilst the temporal eigenvectors are represented by the columns of U, i.e. the ith-column of V is $A^i, i = 1, 2, \dots, N$. The POD spatial modes φ^i are then constructed from the projection of the eigenvector A^i corresponding to the eigenvalue λ^i as:

$$\varphi^i = \frac{\sum_{n=1}^{N} A_n^i w'^n}{\left\| \sum_{n=1}^{N} A_n^i w'^n \right\|} \tag{13}$$

The notation $\| \cdot \|$ is described as $\|R\| = \sqrt{R_1^2 + R_2^2 + \cdots + R_M^2}$. The temporal coefficients a_i, also known as POD coefficients, are calculated by projecting the fluctuating component onto the POD modes, i.e. $a_i^n = \Psi^T w'^n$, where $\Psi = \begin{bmatrix} \varphi^1 & \varphi^2 & \cdots & \varphi^N \end{bmatrix}$. The individual energy coefficients ζ^i and cumulative energy coefficients η^i, are defined as:

$$\zeta^i = \frac{\lambda^i}{\sum_{i=1}^{N} \lambda^i} \tag{14}$$

$$\eta^i = \frac{\sum_{i=1}^{r} \lambda^i}{\sum_{i=1}^{N} \lambda^i} \quad r \leq N \tag{15}$$

where ζ^i denotes the fraction of total energy contained in the ith mode and η^i denotes the proportion of the total energy contained in the first i modes.

Following the snapshot POD method, if the first r modes contain the bulk of the total energy of the flow, then a Reduced Order Model (ROM) of the flow can be effectively used to reconstruct the spatial distribution at any selected time step. The reconstructed field (W_R) can then be given by using the time-averaged velocity $\overline{W}$ plus the truncated POD expansion with r number of modes, as follows:

$$W_R(x_i, t) = \overline{W}(x_i) + \sum_{i=1}^{r} a_i(t)\varphi^i(x_i) \tag{16}$$

According to Sirovich [44], the selective POD modes (or r-POD modes) must satisfy at least $\eta^i \geqslant 90\%$.

3. Results

3.1. Instantaneous flow field

The vortical structures developed behind the horizontal cylinder for the all submergence cases simulated are shown in Figs. 2 and 3 with contours of normalised spanwise vorticity $(\omega_y = \partial u/\partial z - \partial w/\partial x)$ over the xz-plane. In the deepest submergence $(Fr = 0.26)$, the free surface is found well-above the cylinder without causing any noticeable disturbance which allows the von-Kármán vortex street to develop and be convected downstream as shown in Ouro et al. [6]. Due to the considered gap ratio of $G/D = 0.5$, the bottom ground limits the generation of the lower shear layer off the cylinder and vortical structures,
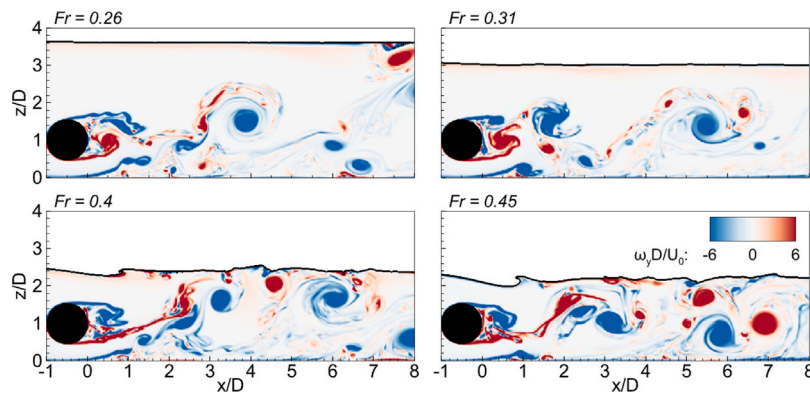
Fig. 2. Contours of normalised vorticity over a vertical plane at the middle of the spanwise domain length comparing the simulated cases with $Fr = 0.26$, 0.31, 0.40 and 0.45. The free surface is depicted as a solid black line.
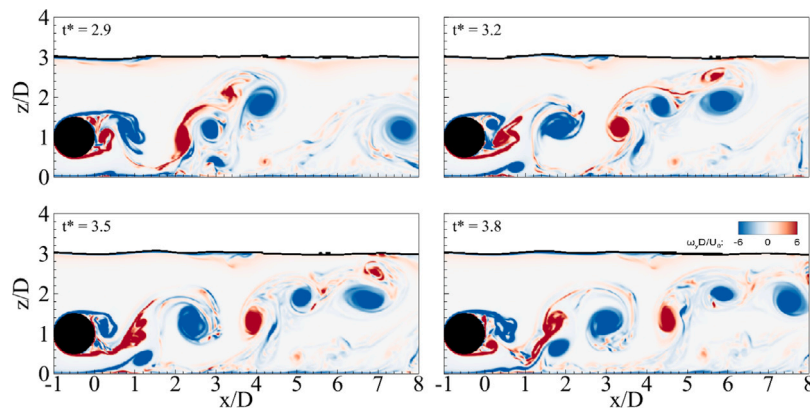

Fig. 3. Contours of normalised vorticity behind the cylinder for the case: $Fr = 0.31$, at four instants normalised by the peak frequency $t^* = 2.9$, 3.2, 3.5, and 3.8. The free surface is depicted as a solid black line.
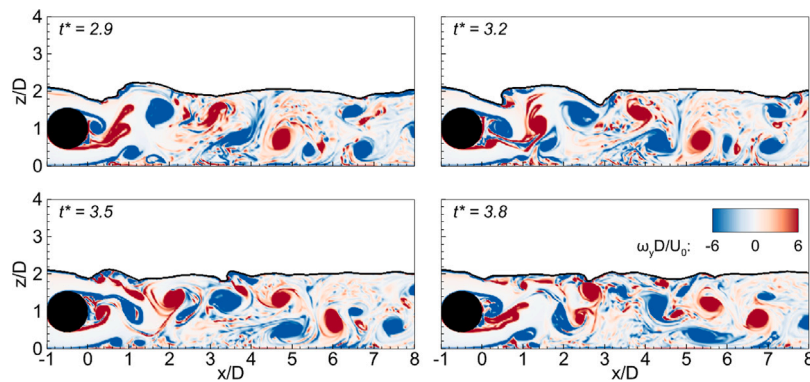

Fig. 4. Contours of normalised vorticity behind the cylinder for the shallowest case: $Fr = 0.53$, at four instants normalised by the peak frequency $t^* = 2.9$, 3.2, 3.5, and 3.8. The free surface is depicted as a solid black line.

suppressing the symmetry in the vortex shedding mechanism leading to a different von-Kármán street compared to unbounded cylinder flows [46]. Decreasing the water depth to $h/D = 1.5$ ($Fr = 0.31$) leads to a slight influence of the water depth reflected from small free-surface variations whilst the von-Kármán vortices follow similar trajectories to those at $Fr = 0.26$.

As the submergence ratio decreases further to $h/D = 0.9$ ($Fr = 0.40$), the free-surface starts to drop shortly downstream of the cylinder and its close location to the cylinder's lee side affects the vortices shed. This can be observed from the vorticity contours for this case in which the vortices reach a vertical height of $z/D \approx 2.4$ shortly after being shed. This interaction induces a quicker loss of coherence of the von-Kármán vortices. Moving to a higher Froude number of 0.45 ($h/D =$

0.7), the interaction between the free surface and the wake's vorticity becomes stronger, and at $x/D = 1$ a hydraulic jump occurs due to the very shallow water conditions of the overtopping flow. For this case, the wake dynamics behind the cylinder exhibit irregular flow patterns. The upper large-scale vortices are distorted when interacting the free surface, which then break up into small eddies near the air–water interface, whilst those vortices moving at the bottom of the water column, e.g. ground vortex (GV), dissipate further downstream (Fig. 2).

Fig. 3 shows the vorticity field for the case simulated at $Fr = 0.31(h/D = 1.5)$ during four time instants covering the time range of $t \cdot f_p \in [2.9, 3.8]$, with t denoting time and f_p is the vortex-shedding frequency. At the normalised instant time of $t^* = t \cdot f_p = 2.9$, the von-Kármán vortices first move upwards due to the effect of the interaction

of the GV and the vortical structure generated behind the cylinder, and subsequently convected downstream by the mean flow in the direction parallel to the free surface, as seen at $t^* = 3.2$. Advancing in time, at $t^* = 3.5$, the developing vortices reach a maximum vertical height of $z/D \approx 3$ at about seven diameters downstream of the cylinder. Their proximity to the upper boundary of the free-surface can lead to alterations in the wake dynamics when compared to unbounded or lower Froude number scenarios. At $t^* = 3.8$, the vortical structures shed over at the lower shear layer are merged with the GV.

Fig. 4 shows the vorticity field for the shallowest case simulated at $Fr = 0.53$ ($h/D = 0.5$) during the four time instants. At the normalised instant time of $t^* = 2.9$, the surface deformation is quite substantial and the flow acceleration between the cylinder and free-surface layer has a direct impact on vortex formation downstream of the cylinder. The vorticity contours show that the vortical structures lose coherence shortly after being shed, with a hydraulic jump formed due to the very shallow flow over the cylinder leading to a marked water-depth drop behind the cylinder compared to its upstream value. Advancing in time at $t^* = 3.2$, the vortices shed in the cylinder wake are seen to merge with the ground vortices before they get diverted upwards approaching the free surface, triggering significant variations in water depth downstream of the cylinder, i.e. $x/D \approx 3$ (Fig. 4). As a consequence of this interaction, the turbulent mixing increases resulting from a higher interaction of the free-surface effects with the bulk flow. At $t^* = 3.5$, the significant depression in the water surface behind the cylinder is recovered, allowing the vortices shed from the upper side of the cylinder to extend further downstream with a lower interaction with the free surface which, in consequence, led to an increasingly complex flow dynamics far downstream of the cylinder. Moreover, the top shear-layer vortices are not only affected by the vicinity of the free surface, but they are also amalgamated with the ground vortices. These structures dissipate at a faster rate than those found in deeper flow conditions, making the turbulent wake to become more irregular ($t^* = 3.8$, Fig. 3).

3.2. Turbulent momentum exchange

Fig. 5 shows the distribution of the vertical Reynolds shear stress $(-\langle u'w' \rangle)$ contours for the different submergence cases to showcase the turbulent momentum exchange in the cylinder's wake. At $Fr \leq 0.40$, the vertical Reynolds shear stress at the lower side of the cylinder in the near wake region is shifted downstream due to the flow acceleration coming from the bottom gap. In contrast, the upper side of the cylinder in the near wake region appears unchanged for $Fr \leq 0.40$, which can be attributed to limited effect of the free-surface to alter the vortex shedding dynamics at this location. As the Fr increases, the free-surface proximity is shown to limit the longitudinal expansion of regions of high $-\langle u'w' \rangle$ and their vertical location being pushed to towards the bottom wall. For the highest Fr cases the standing wave shown in the mean free-surface profile introduced an additional contribution to momentum exchange, especially for the highest Froude number case. Overall, contours of $-\langle u'w' \rangle$ indicate that until $x/D = 2$ the turbulent momentum exchange in the wake is large for all submergence levels.

Vertical profiles of $-\langle u'w' \rangle$ at four downstream locations along the water depth are presented in Fig. 6 for the five simulated cases Fig. 6 shows that in the near wake region, i.e. at $x/D = 0.5$, all cases compute similar turbulent momentum exchange values in the bottom half blow the cylinder's centre ($z/D \leq 1.0$) while the values along the top shear layer at approx. $z/D = 0.85$ peak at Fr 0.40. This upper shear-layer maxima of $-\langle u'w' \rangle$ significantly drops at $x/D = 1.5$, with the vertical location of the largest value at $Fr = 0.53$ decreases to $z/D = 1$ due to the influence of the free-surface in the turbulent momentum exchange region. Maximum values of $-\langle u'w' \rangle$ in the lower shear layer at the latter location is again observed at $Fr = 0.40$. Further downstream of the cylinder at $x/D = 2.5$, the vertical Reynolds shear stress distribution varies with the submergence level, with a notable turbulence level decay seen for $Fr \geq 0.31$. At $x/D = 3.5$ and 4.5 show that the largest momentum exchange at cylinder height is for the shallowest submergence.
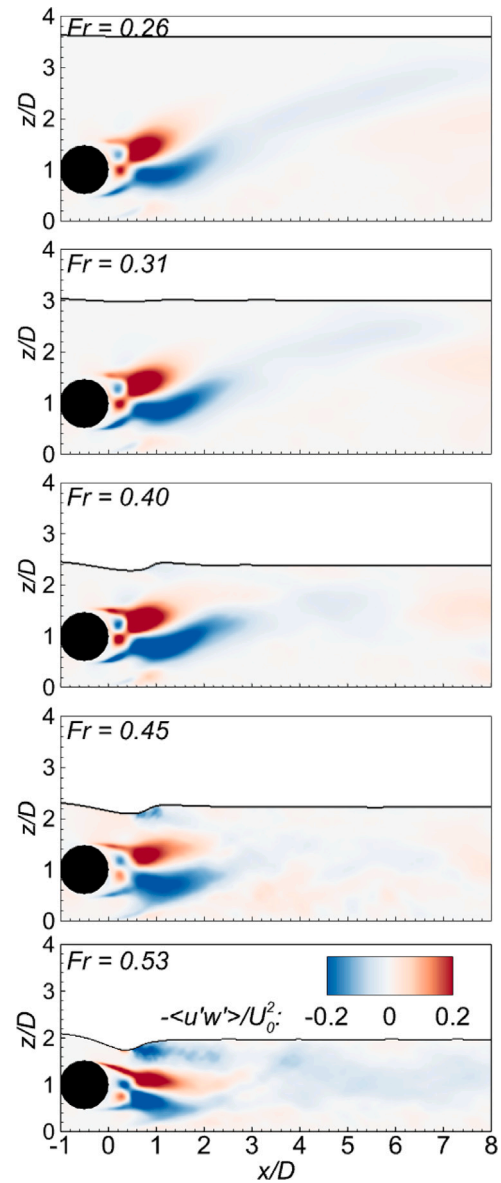

Fig. 5. Contours of normalised vertical Reynolds shear stress $(-\langle u'w' \rangle / U_0^2)$ comparing the cases at $Fr = 0.26$, 0.31, 0.40, 0.45 and 0.53. The free-surface is depicted as a solid black line.

3.3. Proper-Orthogonal Decomposition (POD) analysis

Details about how the instantaneous wake characteristics vary with increasing submergence ratios are analysed in this section using the POD methodology.

3.3.1. Snapshots dependence validation

The sensitivity of POD to the temporal duration of the LES velocity dataset is studied comparing the energy contribution of the eigenvalues as a function of the number of snapshots. Fig. 7a shows the energy content of the first 100 modes when using 200, 400, 800 and 900 snapshots, for the case at $Fr = 0.26$, at a fixed time step of $0.006\ s$ between two successive snapshots, which is equivalent to approximately two, four, seven and eight vortex shedding cycles, respectively. The energy contribution of the four datasets show minor variations in the first six POD modes, while differences become more evident after the POD mode 15. As the energy variation is small when increasing the sampling time from 800 to 900 snapshots, thus a total of 900 snapshots are
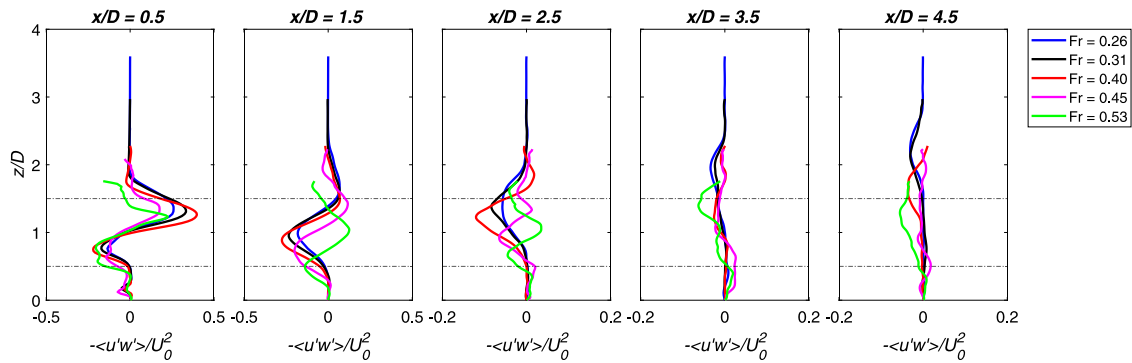
Fig. 6. Vertical profiles of normalised vertical Reynolds shear stress $\left(-\langle u'w'\rangle\right)/U_0^2$ at different locations downstream of the cylinder for the different simulated cases. The cylinder position is depicted as horizontal dot–dash lines.
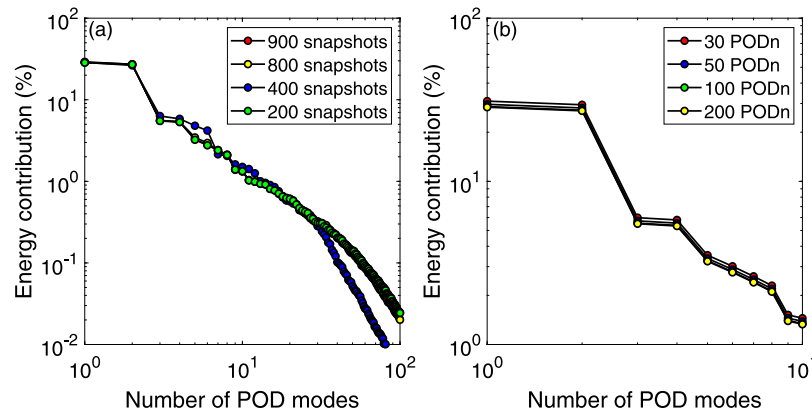

Fig. 7. Sensitivity analysis of the energy contribution when adopting (a) different number of snapshots based on 100 POD modes and (b) increasing POD modes with 900 snapshots.

adopted in the following analysis. For this selected number of snapshots 100 POD modes are originally used. However, sensitivity to the number of POD modes used in the snapshot POD decomposition is examined in Fig. 7b, showing the variation of the energy contribution of the first 10 POD modes when increasing the total number of POD modes from 30 to 200 in the SVD decomposition. Only significant differences in the energy contribution are observed in the first 10 modes with a slightly larger energy prediction when using 30 POD modes compared to when more modes are used, whilst almost no significant variations in the relative energy are seen adopting 100 or 200 POD modes. Hence, 100 POD modes based on 900 snapshots (eight vortex shedding cycles) are deemed adequate to perform the POD analysis for the present study.

3.3.2. Energy contribution of POD modes

The relative energy of each POD mode and consequent cumulative energy for the simulations with different Froude numbers is shown in Fig. 8. The contribution of POD modes to the total energy seems to follow a similar distribution among all Fr cases. The first two POD modes have similar relative energy with the largest overall contribution, as these correspond to the energetic large-scale von-Kármán vortices shed by the cylinder (as shown later in the following section). The energy contained in higher POD modes progressively decreases as they represent the contribution from small-scale turbulent structures [47,48]. As seen in Fig. 8 a, the first two modes account for 56.0%, 52.59%, 54.24% and 42.78% of the total energy for those cases at $Fr = 0.26$, 0.31, 0.40 and 0.45 respectively, whist this notably decreases to 26.8% at $Fr = 0.53$. Such result variation reflects that free-surface effects under shallower flow conditions leads to a loss of coherence, or energy, from the dominant von-Kármán-like vortices, directly reducing the energy of the eigenvalues of modes 1 and 2. In all submergence cases, mode 1 has an energy contribution of about 1% larger than mode 2.

Fig. 8b compares the cumulative energy for the different Fr cases, which is similar for the deepest conditions at $Fr = 0.26$, 0.31 and 0.40. Conversely, there are large differences between the shallower conditions at $Fr = 0.45$ and 0.53 with a noticeable deviation from the other deeper cases as modes 1 and 2 have a lower energy when shallowness increases. Specifically, the first 25 POD modes contain around 80% and 75% of the total energy for the cases at $Fr = 0.45$ and 0.53 respectively, compared to an average value of 90% found for the deeper cases. This implies that for shallower conditions more POD modes are required to account for the same amount of energy, indicating that free-surface effects notably impact the vortex shedding nature behind the cylinder when Fr is larger than 0.4 at the present gap-to-diameter ratio of 0.5 (as shown in Figs. 2 and 4).

3.3.3. POD spatial modes

To further quantify the impact of relative submergence on the wake dynamics, the POD spatial modes and corresponding temporal coefficients are analysed. The most energetic POD modes are often paired, i.e. consecutive modes have a similar energy contribution, spatial and temporal modes, only differing by a phase shift [49]. This is observed in Figs. 9 and 10 with the first six POD spatial modes in which modes 1 and 2 are denoted as the pair 1, while pair 2 corresponds to modes 3 and 4, and pair 3 to modes 5 and 6. Irrespective to the submergence level, i.e. Froude number, the coherent regions in the first two modes have similar spatial structure that capture large-scale flow structures. For the deeper submergence cases, the observed spatial modes retain a similar distribution to other POD studies for flow behind cylinders [50, 51] despite the close proximity to the bottom surface affecting the wake dynamics [6]. Transitioning to shallower flow conditions impacts the coherence of the most-energetic wake structures, as with increasing Fr the turbulent structures from the first pair of modes decreased in
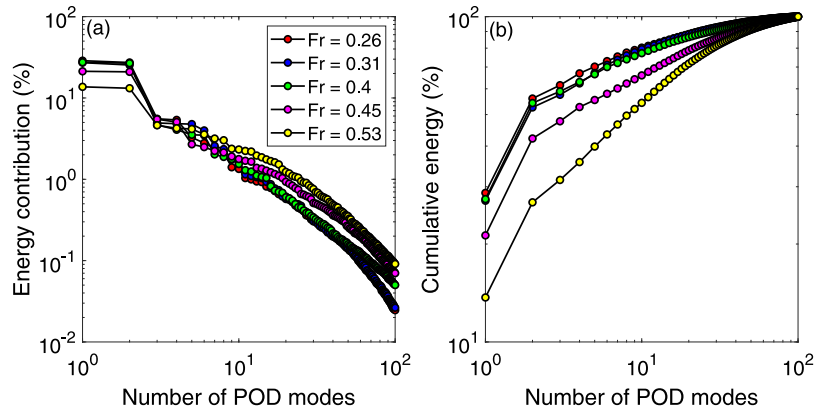
Fig. 8. Comparison of the (a) energy contribution and (b) cumulative value for the 100 first POD modes for the different submergence cases.
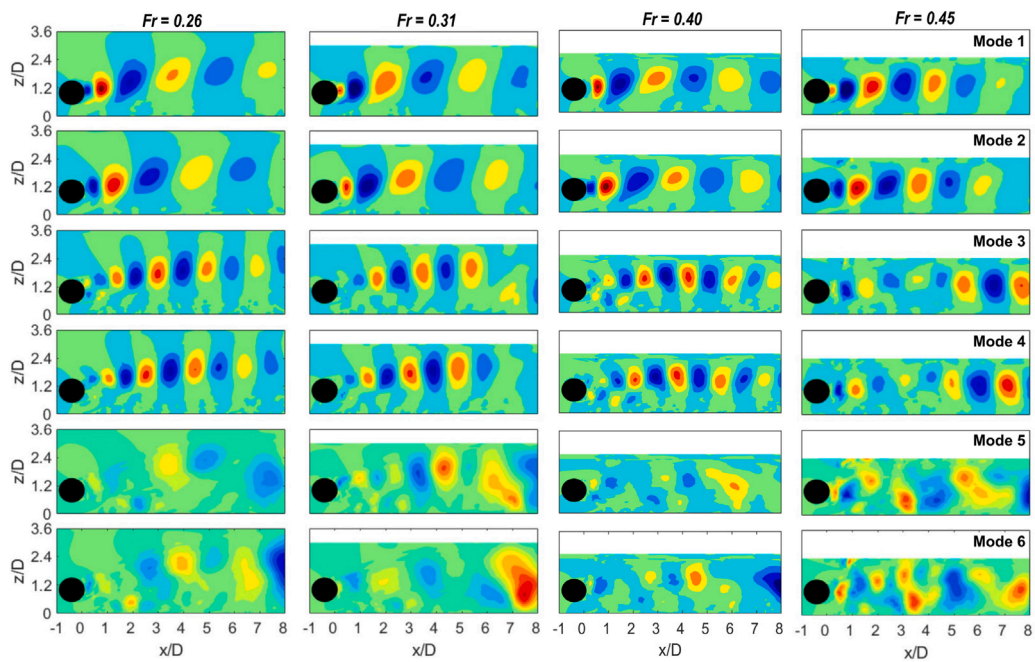

Fig. 9. First six POD spatial modes obtained for cases with Fr = 0.26, 0.31, 0.40, and 0.45.
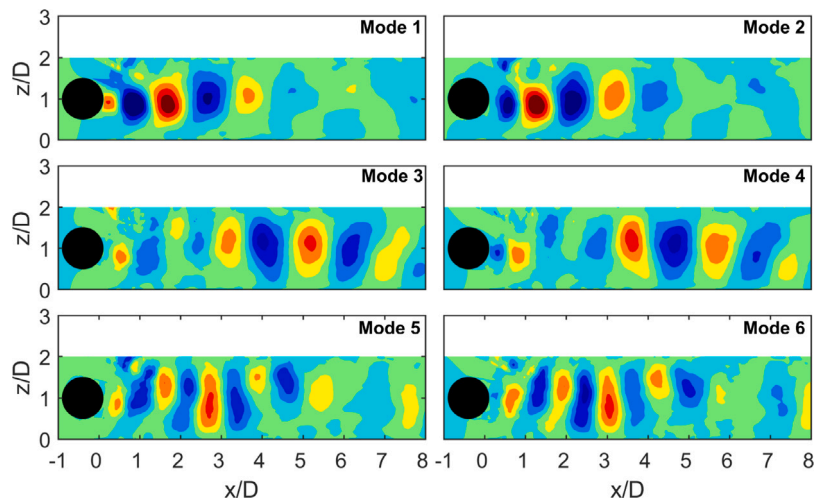

Fig. 10. Six POD spatial modes obtained for the shallowest case: Fr = 0.53.
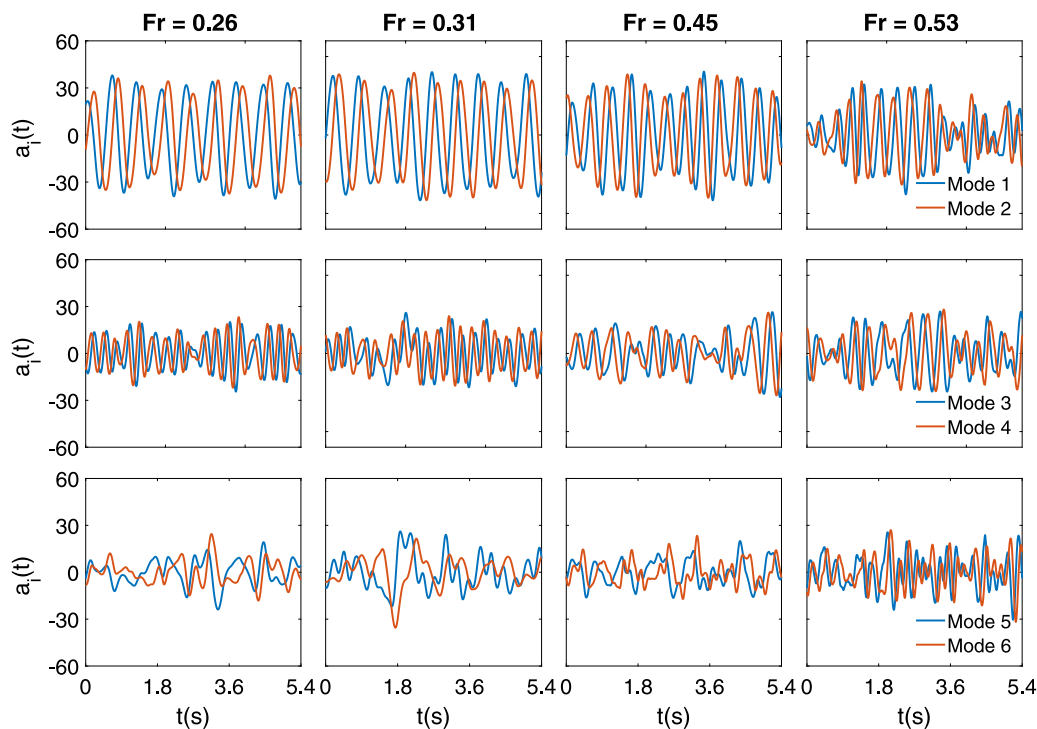
Fig. 11. Temporal coefficients of the first six POD modes obtained for the cases with $Fr = 0.26$, 0.31, 0.45 and 0.53.

longitudinal and vertical size as there is a limited vertical expansion due to the free-surface proximity.

The second pair of POD modes captures smaller scale flow structures whose contribution to the overall energy is lower than the first pair (Fig. 8). Modes 3 and 4 at $Fr = 0.26$, 0.31 and 0.40 are almost identical, suggesting that the vortex shedding has a negligible impact from the free-surface. Conversely, in the cases at $Fr = 0.45$ and 0.53, this pair of modes losses its spatial coherence with smaller scales in the region closer to the lee-side of the cylinder whilst larger structures are observed in the far-wake. The third pair at $Fr = 0.26$, 0.31, 0.40 and 0.45 exhibits a less clear spatial distribution capturing a range of flow structures, especially for the deepest flow conditions, which is attributed to the energy content of these modes. Alternatively, for the $Fr = 0.53$ case the energy contribution of pairs 1 and 2 is similar and so are the coherent regions of velocity fluctuations in their POD modes (Fig. 10). It appears that pair 1 shows coherent structures until a downstream location of $x/D = 4$ after which these vanish, whilst in pair 2 this pattern is reversed, i.e. coherent regions are seen after $x/D = 4$. The third pair exhibits a rather well-defined distribution compared to the other cases. These results suggest that the large-scale von-Kármán vortices developed in cases with high Froude numbers, i.e. at low submergence, lose coherence more rapidly due to the free-surface impact.

3.3.4. POD temporal coefficients and associated Strouhal number

The temporal coefficients of the six POD modes whose spatial distribution is presented in Figs. 9 and 10 are now presented in Fig. 11 with the exception of the case at $Fr = 0.40$ (For brevity, presented in Appendix B), which outline the phase difference in the temporal oscillation of the modes within the same modal pair. The temporal coefficients of the first pair exhibit the highest amplitudes compared to the other two pairs (modes 3 to 6) due to their higher energy contribution and spatial coherence, linked to the large-scale von-Kármán vortices. For cases at $Fr = 0.45$ and 0.53, the first pair features a periodic oscillation of the temporal POD coefficients but with an irregular amplitude, especially for the shallowest submergence case, suggesting that the periodic shedding of von-Kármán vortices is most

impacted by the free-surface for this case. Modes 1 and 2 are out of phase by less than a quarter wavelength for cases with $Fr = 0.26$, 0.31 and 0.40, representing shifted structures in the advection direction by a distance corresponding to their phase difference. However, for higher Fr, modes 1 and 2 exhibit a smaller phase difference and a reversed temporal behaviour compared to lower Fr, which agrees with their corresponding spatial structures (Figs. 9 and 10). This again reflects how the free-surface drives the motion of vortical structures downstream of the cylinder.

The second pair of modes also exhibits a sinusoidal shape with a lower, less regular amplitude that is twice that of the first pair at $Fr = 0.26$, 0.31 and 0.40, reflecting harmonics of the von-Kármán vortex shedding. Conversely, for higher Froude numbers, the oscillations exhibit a more irregular variation. Irrespective of the submergence level, the temporal coefficients from the third pair of modes show an uneven signal with drastic changes in amplitude, linked to non-periodic flow motions depicted by the uneven spatial correlation of their spatial modes seen in Figs. 9 and 10. For the shallowest case, the third pair of modes retains some degree of correlation in its frequency to pairs one and two, which is linked to their closer energy content (Fig. 8).

Further identification of the relationship between the POD eigenmodes and flow structures is provided with the Power Spectral Density (PSD) computed from the first six POD temporal coefficients (Fig. 11), which are presented in Fig. 12 (see Appendix B for $Fr = 0.40$) together with the corresponding Strouhal number for each case. The latter is calculated as $St = f_p D / U_0$, with f_p corresponding to the vortex shedding frequency calculated from the time series of vertical velocities at $x/D = 2.1$, $z/D = 1.5$. The Strouhal number associated to cases at $Fr = 0.26$, 0.31, 0.40, 0.45 and 0.53 are 0.29, 0.31, 0.32, 0.41 and 0.48, respectively. The first harmonic at a frequency of twice St is also included in Fig. 12. Irrespective of the submergence case, the spectra of the temporal coefficients from the first two modes show a dominant peak that corresponds to the vortex shedding frequency, indicating that these POD modes represent to the dominant von-Kármán vortex shedding. In all cases, the two modes corresponding to the same pair feature an energy peak at a given frequency as they are associated to the same flow structures.
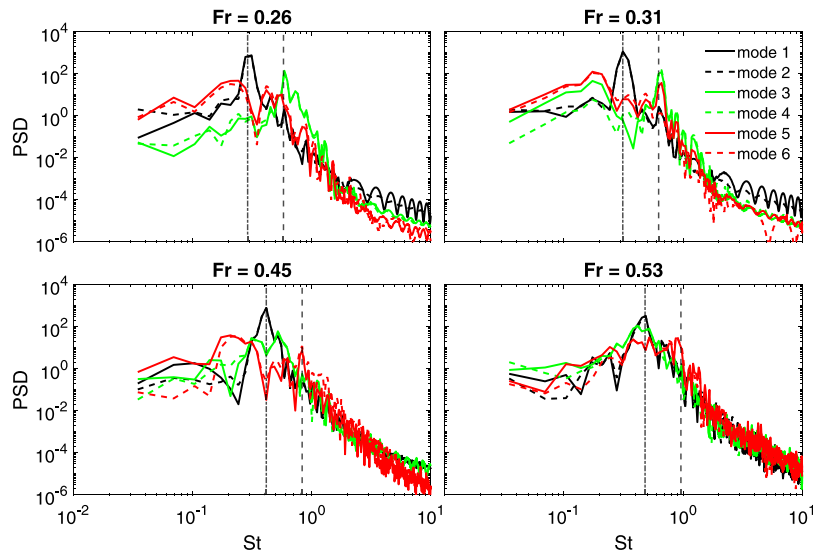
Fig. 12. Power spectral density (PSD) of the temporal coefficients from the first six POD modes obtained for the four submergence cases. The dot-dashed line indicates the Strouhal number (St) frequency associated to the periodic vortex shedding and the dashed line indicates its first harmonic ($2St$).

The amplitude of the spectral energy peak at the dominant St frequency reduces for higher POD modes as their energy content is also smaller, with their pattern changing with the submergence level. At $Fr = 0.26$, the pair one peaks at St, pair two at $2St$ but pair three does not have a marked peak with its maximum at a frequency slightly lower than St. Conversely, at $Fr = 0.31$, the pair one again peaks at St and pair two at $2St$ but modes 5 and 6 have an increased energy content at lower frequencies which is almost analogous to the spectral distribution from pair three. The second pair still peaks at $2St$ for $Fr = 0.40$, whereas the third pair has a similar feature of its counterpart at $Fr = 0.26$. Decreasing the submergence depth at $Fr = 0.45$, the pairs two and three have a reversed PSD distribution as that at lower Fr cases due to the close energy content of modes in these pairs shown in Fig. 8. Finally, for the lowest submergence at $Fr = 0.53$, the pairs one and two peak at St whilst pair three does at $2St$ but without a defined band of the frequencies.

3.3.5. Lissajous curves

The link between POD modes is provided in Fig. 13 with the correlation between the temporal coefficient from the first mode (a_1) with those from modes two to six (a_i). These Lissajous plots depict the phase difference between modes. The first two modes clearly show that the correlation trajectory of $a_1 - a_2$ exhibit circular shape, which indicates these modes have a close amplitude and frequency. Such almost linear correlation between coefficients $a_1 - a_2$ allows to fit a representative circle, e.g. using the least squares method, depicted by a solid line in Fig. 13.

The linear correlation between the first two modes has the lowest errors for cases at $Fr = 0.26$ and 0.31 when the shedding of vortical structures are more coherent in space at time. As submergence decreases at $Fr = 0.45$, the $a_1 - a_2$ data points become more scattered and deviated from the fitting circle. For the smallest submergence case, the data exhibit a substantial error from the solid circle as the vortex shedding dynamics are highly altered due to the very shallow flow conditions, which would render difficult to the flow field reconstruction if only the first two POD modes were used. The scatter plots of $a_1 - a_4$ at $Fr = 0.26$ and $a_1 - a_3$ at $Fr = 0.31$ (Fig. 13), indicate that modes 3 and 4 have half the amplitude, twice the dominant frequency compared to mode 1 [52]. All the other trajectories do not exhibit a clear temporal correlation with a dominant frequency. These results can be seen in Fig. 12 in which low-energy modes comprise different peaks with lower magnitudes that may cause some modulations in these frequencies [53,54].

3.4. Velocity field reconstruction

A reduced-order model (ROM) based on the POD spatial modes and temporal coefficients can be built to represent the velocity field in a cost-effective way [45,55]. As the ROM accuracy depends on the number of POD modes adopted, the normalised instantaneous velocity (w) and its fluctuation component (w') obtained from the LES (deemed as the true solution) at a given time step and that predicted from the ROM (Eq. (16)) are shown in Figs. 14 and 15, adopting the first 2, 10, 20, and 100 POD modes for four submergence cases. The associated absolute error from the ROM-predicted velocity fluctuation compared to the LES value (error = $W_{LES} - W_{ROM}$) is also included.

The ROM based on the first two modes accounts for the two most energetic modes associated to the von-Kármán vortices, which represent a total energy content in the range of 42%–56% for cases with $Fr < 0.53$ while about 27% for the shallowest submergence case (Fig. 8). Figs. 14 and 15 show that adopting two POD modes in the ROM leads to large errors, especially at $Fr = 0.53$ in which the first pair of POD modes provide the lowest energy contribution. Increasing the number of POD modes in the ROM allows to account for flow structures that are less energetic but whose overall energy contribution is not negligible (Fig. 8a). When using 20 modes for the ROM, the reconstructed velocity field is close to the LES field for cases with $Fr < 0.45$ as these account for almost 90% of the total cumulative energy contribution (Fig. 8b) and less than 80% and 70% for $Fr = 0.45$ and 0.53, respectively. Consequently, the latter cases exhibit larger errors from the 20-mode-based ROM. Adopting 100 modes provides an increased accuracy from the ROM capturing flow structures both in the near- and far-wakes, leading to a 1% error at $Fr \leq 0.45$, while an spatially average error of 2% is found for cases at $Fr = 0.45$ and 0.53. This deviation from the ROM accuracy suggests that the impact of the free-surface on the cylinder wake dynamics can be quantified in the POD analysis by the number of modes that would contribute to, at least, 90% of the energy content [56]. For instance, in the present cases, the reconstruction of the velocity field at $Fr = 0.26$ requires around 20 modes for a cumulative 90% of the total turbulent kinetic energy, while to capture the same amount of energy at $Fr = 0.53$, about 50 POD modes are required. Overall, a ROM based on 100 POD modes provides an excellent agreement with the LES for all cases.

To evaluate the ability of the ROM in reproducing instantaneous velocities over time, Fig. 16 shows the instantaneous vertical velocity (w) time-series at $x/D = 3.5$, $z/D = 1.2$, i.e. in the upper shear
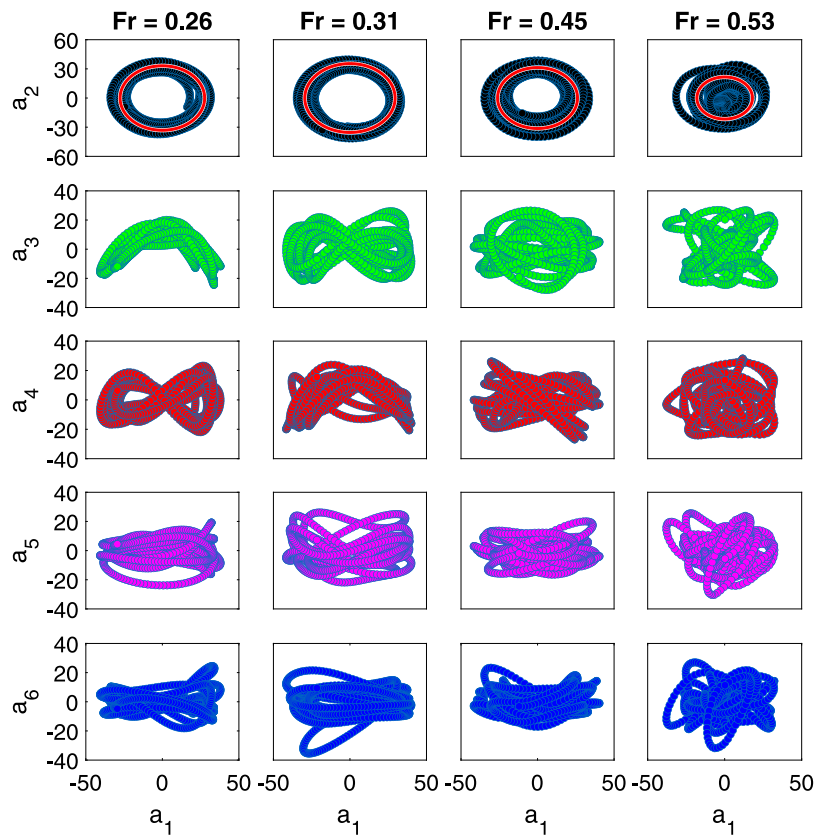
Fig. 13. The Lissajous plots of the first six POD coefficients for cases with Fr = 0.26, 0.31, 0.45 and 0.53. The linear fit with a circular curve shown in the first row.
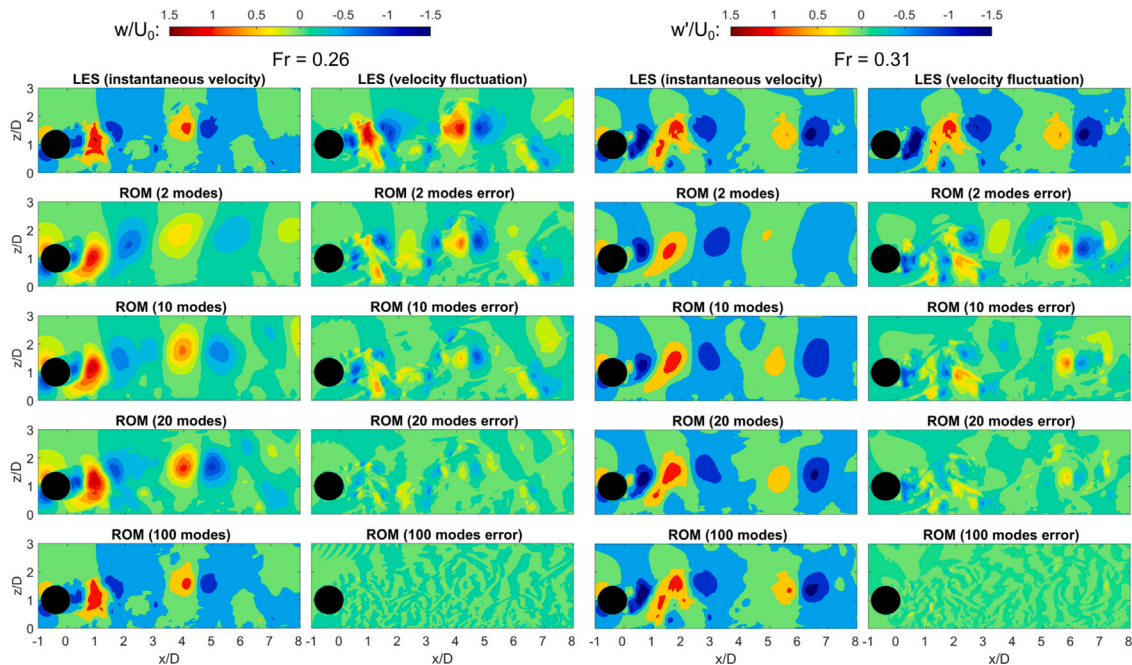

Fig. 14. Comparison between the LES (first row of figures) velocity data with those reconstructed with the ROM based on an increasing number of POD modes for Fr = 0.26 (left) and 0.31 (right).

layer of the cylinder in which von-Kármán vortices pass through when shed [6], from the LES and those reconstructed using the ROMs with increasing number of POD modes for four submergence levels. Overall, convergence of the ROM predictions is observed when increasing the

number of POD modes, requiring almost 100 modes in all submergence cases to capture the low- and high-frequency oscillations of the velocity. Adopting less than 10 modes in the ROM does capture the low-frequency oscillations but without an appropriate amplitude,
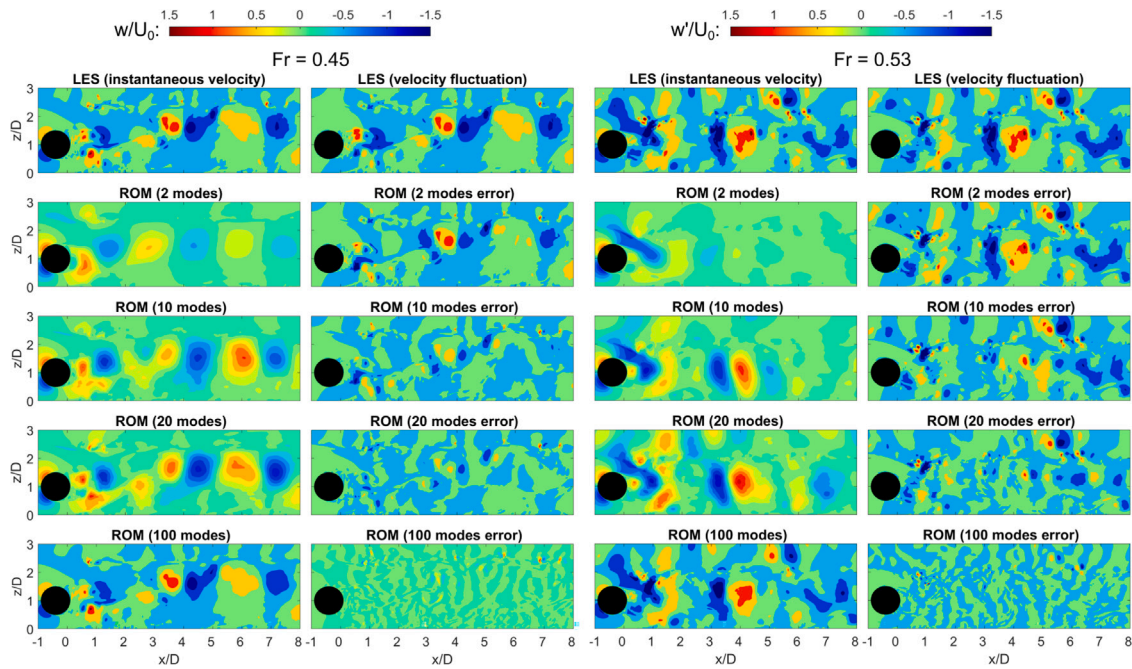
Fig. 15. Comparison between the LES (first row of figures) velocity data with those reconstructed with the ROM based on an increasing number of POD modes for $Fr = 0.45$ (left) and 0.53 (right).
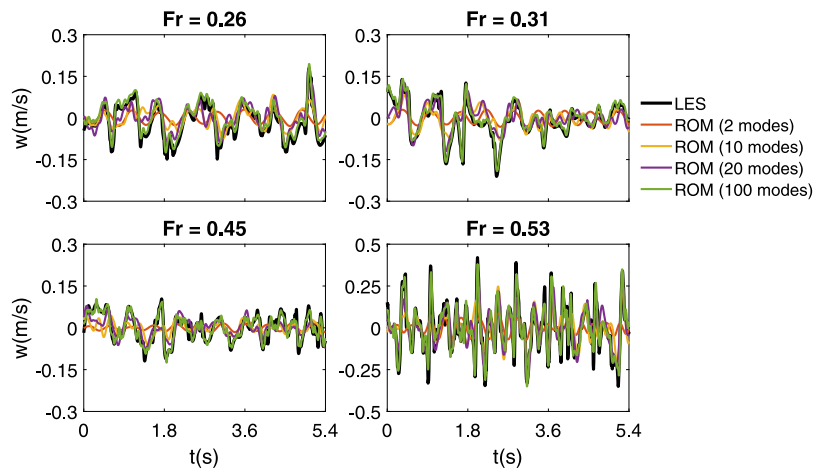

Fig. 16. A comparison between the instantaneous velocity obtained from the LES and the ROMs over the time history adopted for the POD analysis for the different Froude numbers.

indicating that the contribution from higher POD modes is still required to effectively capture the flow dynamics.

The sensitivity of the ROM to the number of POD modes adopted is presented in Fig. 17 with the root-mean-square (rms) error of the reconstructed vertical velocity field at a single time step over the xz-plane (Fig. 15) or at a point over time (Fig. 16). Results shown in Fig. 15a indicate that at $Fr \leq 0.45$ an appropriate velocity reconstruction can be obtained adopting a small number of POD modes, while a large number of POD modes is required for shallower cases to achieve lower ROM errors. Thus, the wake dynamics at higher Fr are driven by a wider range of flow structures needed to be included in the flow reconstruction. Fig. 17b shows the rms of the velocity time series reconstruction at the selected point. For the shallowest case at $Fr = 0.53$, the minimum reconstruction error obtained with 100 POD modes is over 2.5%, whilst this error value can be attained with approx. 60, 50 and 27 POD modes at $Fr = 0.45$, 0.31 and 0.26, respectively. Note that this point is close to the free-surface in the shallowest submergence (Fig. 4) and thus its impact challenges the ability of the ROM to fully

capture the instantaneous velocity field. Nevertheless, an error of 1% allows for a very precise reconstruction solution, while an error of less than 3% can be deemed adequate for a low-dimensional ROM [57].

3.5. Analysis of the spectral energy decay

Fig. 18 presents an analysis of the Power Spectral Density (PSD) computed from vertical velocity fluctuations at a point located at $x/D = 1.1$ and $z/D = 1.5$, which is in the cylinder's wake and close to the free-surface, for Fr of 0.31, 0.45, and 0.53. The first set of PSD plots (a–c) is obtained from 48 vortex-shedding cycles computed from the full LES, whereas the second sub-set (d–f) is obtained over a shorter time series of eight vortex-shedding cycles used to construct the ROM based on the first 2, 10, 20, and 100 modes. The spectral analysis in Fig. 18a–c exhibits a clear energetic region in the production range corresponding to the energetic eddies emanating periodically from the cylinder over a frequency band close to the shedding frequency. This is most prominent at $Fr = 0.31$ (Fig. 3), while less pronounced peaks
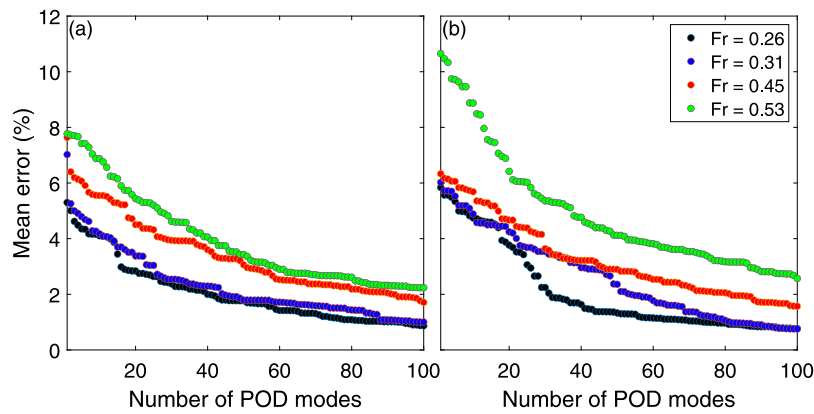
Fig. 17. The mean error plot of the reconstructed velocity (a) over a vertical plane at a single snapshot and (b) at $x/D = 3.5$, $z/D = 1.2$ for all snapshots as a function of the number of POD modes.
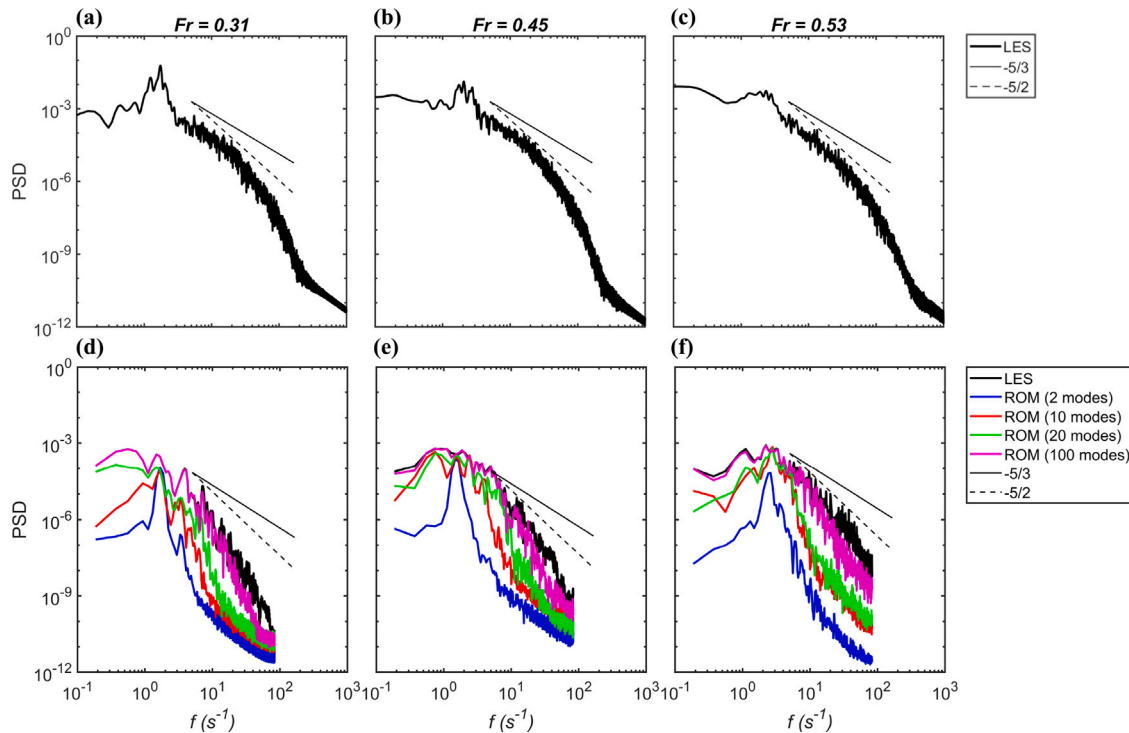

Fig. 18. Power spectral density (PSD) of the vertical velocity fluctuation (w') obtained at a point ($x/D = 1.1$ and $z/D = 1.5$) from LES long time series (a–c) and truncated time series from LES and POD-based ROM at $Fr = 0.31$, 0.45, and 0.53.

are observed at higher Fr, suggesting more irregular vortex shedding patterns (see Fig. 4). At high submergence rates, the inertial sub-range follows the classical $-5/3$ Kolmogorov's slope over a frequency decade up to approx. 20 Hz, after which the decay rate increases with a steeper decay law of $-5/2$. This acceleration in energy decay can be due to excessive dissipation resulting from the distorted free-surface and cylinder proximity to the bottom wall [58] or even turbulence anisotropy [59]. Similar findings have been provided by Zhao et al. [60] for flow past a cylinder close to a free-surface. At $Fr = 0.53$, this $-5/2$ slope provides a closer fit to the energy decay over most of the inertial sub-range and the production range has less energy near the shedding frequency than at $Fr = 0.31$ or 0.45 as the vortices shed have less coherence due to free-surface effects (Fig. 4).

Fig. 18d–f presents the PSD associated with the truncated time series obtained from the full LES and reconstructed POD modes. As the number of modes increases, the associate energy of the PSD increases, with the ROM using 100 modes collapsing with the LES spectrum over the production range up to a frequency of 20 Hz, when the energy

decay starts to accelerate in the full LES (Fig. 18a–c). The truncated time series provides valuable insights into the relationship between the increased amplitude in the PSD and number of POD modes to be adopted for flow field reconstruction, as a criterion to decide how many modes in a ROM shall be adopted.

4. Discussion and conclusions

In this paper, the turbulent flow past a horizontal circular cylinder is resolved using large-eddy simulation to quantify the effect of the proximity to free surface on wake dynamics. Five different relative submergences were considered yielding Froude numbers in the range of 0.26–0.53 for a constant cylinder Reynolds number 13,333 and a bottom gap ratio of 0.5. The instantaneous flow field revealed that the proximity of the cylinder to the bottom wall and free surface significantly influenced the vortex-shedding dynamics with a notable impact on the coherent structures with increasing Froude number. At a low Froude number (Fr) of 0.26, the impact from the free surface
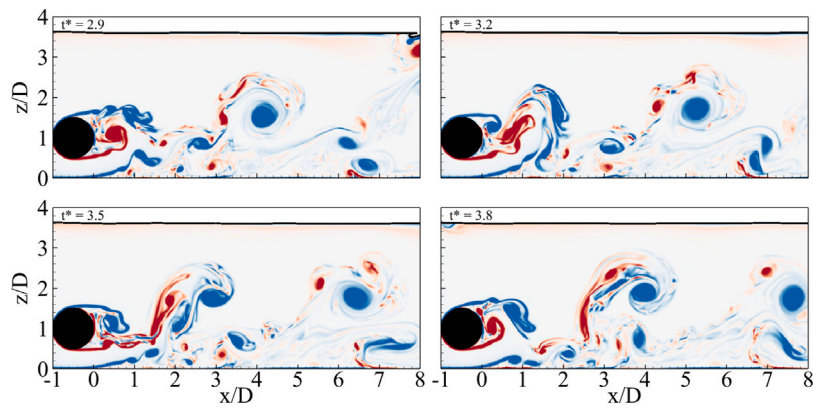
Fig. A.19. Contours of normalised vorticity behind the cylinder for the case: $Fr = 0.26$, at four instants normalised by the peak frequency $t^* = 2.9$, 3.2, 3.5, and 3.8. The free surface is depicted as a solid black line.
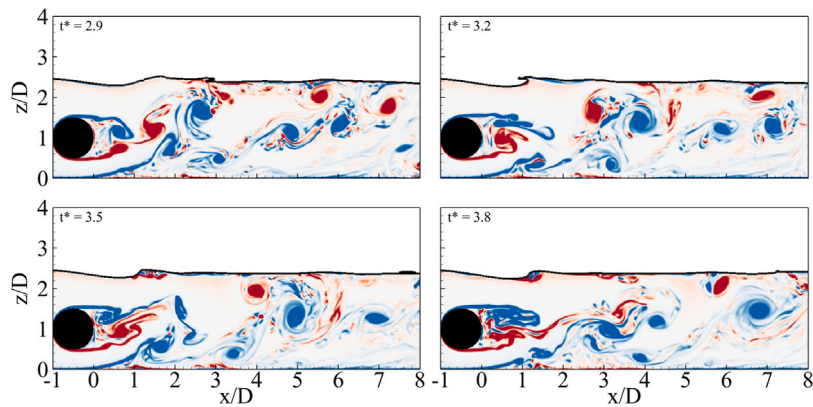

Fig. A.20. Contours of normalised vorticity behind the cylinder for the case: $Fr = 0.40$, at four instants normalised by the peak frequency $t^* = 2.9$, 3.2, 3.5, and 3.8. The free surface is depicted as a solid black line.
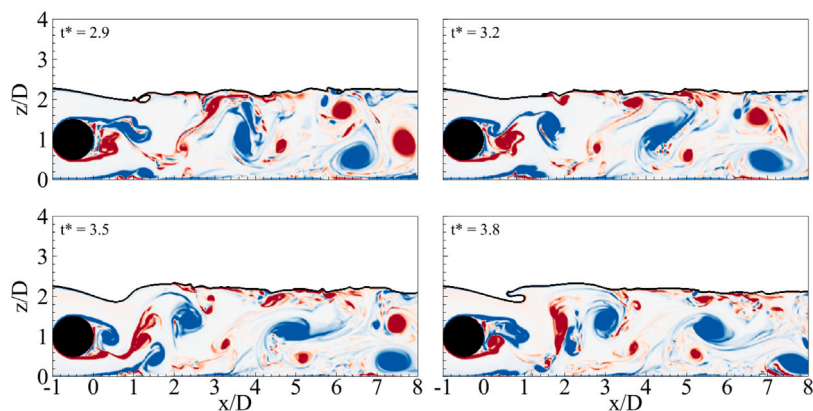

Fig. A.21. Contours of normalised vorticity behind the cylinder for the case: $Fr = 0.45$, at four instants normalised by the peak frequency $t^* = 2.9$, 3.2, 3.5, and 3.8. The free surface is depicted as a solid black line.

on the cylinder wake is deemed negligible as no obvious distortion in the free surface was observed, while the ground proximity affected the symmetry in the vortex shedding mechanism leading to a different von-Kármán street compared to unbounded cylinder flows. As Froude number increased beyond 0.4, substantial free-surface deformations occurred, which significantly suppressed the development of the periodic vortex structures and induced a quicker loss in their spatial coherence.

Proper-Orthogonal Decomposition (POD) was performed based on the vertical velocity fluctuations for all the flow configurations studied. In all cases, POD modes were paired, as the two consecutive odd–even modes had a similar energy contribution and POD spatial mode and

temporal coefficient patterns. The first two modes contributed with more than 42% of the total energy for cases with $Fr \leq 0.45$, whilst at $Fr = 0.53$ these eigenvalues reduced their contribution to almost half due to the influence of the free-surface proximity on the coherent structures. The distribution of POD spatial modes revealed that the first two modes feature the same spatial structure corresponding to large flow structures irrespective to the Froude number. However, their coherence was altered when transitioning to shallower flow conditions, which led to a loss in coherence of the vortices. The POD temporal coefficients for these first two modes exhibited higher amplitudes compared to higher POD modes as a result of their larger energy contribution, although the

amplitude of the former became more irregular with increasing Fr. This indicates that the free-surface proximity directly impacts the periodic shedding of von-Kármán vortices.

The spectra of the POD temporal coefficients of the first pair of modes featured peaks at frequencies corresponding to the dominant structures represented by the Strouhal number (St), namely at 0.29, 0.31, 0.32, 0.41 and 0.48 for cases with Fr = 0.26, 0.31, 0.40, 0.45 and 0.53 respectively. This revealed that the frequency of the flow structures represented by these modes agreed with the von-Kármán vortices shed by the cylinder. Correlation between the temporal coefficient of mode 1 against modes 2 to 6 showed that only the first two modes had a linear correlation. As the Froude number increased, such correlation became more scattered, linked to free-surface effects on the vortex shedding. The velocity fluctuation reconstructed by a Reduced Order Model (ROM) using the first 20 POD modes was deemed enough for obtaining similar vortical structures to those observed from the original large-eddy simulations. For the cases at $Fr \geq 0.45$, the ROM based on the first 20 modes still exhibited a relatively large error, and required a larger number of modes to take into account small scale structures that improved accuracy.

The spectra of the vertical velocity fluctuations from a point in the cylinder's wake exhibit a clear production range with an inertial sub-range following Kolmogorov's $-5/3$ slope at low Froude numbers, whilst a steeper $-5/2$ decay scale is observed for shallower conditions. The spectra from the reduced-order models show that 100 POD modes effectively reproduces the LES spectrum up to a frequency of 20 Hz, whilst adopting less modes only captures the energy at the peak shedding frequency.

The presented results quantified the impact of the free-surface proximity on horizontal cylinder wake dynamics, especially in the coherence of the turbulent structures identified through an extensive POD analysis compared to LES data. Our study also revealed the complexity in modelling shallow turbulent flows, which requires advanced simulation techniques to account for free-surface deformations.

CRediT authorship contribution statement

Fawaz Alzabari: Conceptualization, Methodology, Numerical investigation, Data curation, Formal analysis, Validation, Writing – original draft, Data interpretation, Writing – review & editing. **Catherine A.M.E. Wilson:** Conceptualization, Methodology, Supervision, Data interpretation, Writing – review & editing, Funding acquisition. **Pablo Ouro:** Conceptualization, Methodology, Supervision, Data curation, Formal analysis, Validation, Writing – original draft, Data interpretation, Writing – review & editing, Funding acquisition.

Declaration of competing interest

The authors declare that they have no known competing financial interests or personal relationships that could have appeared to influence the work reported in this paper.

Data availability

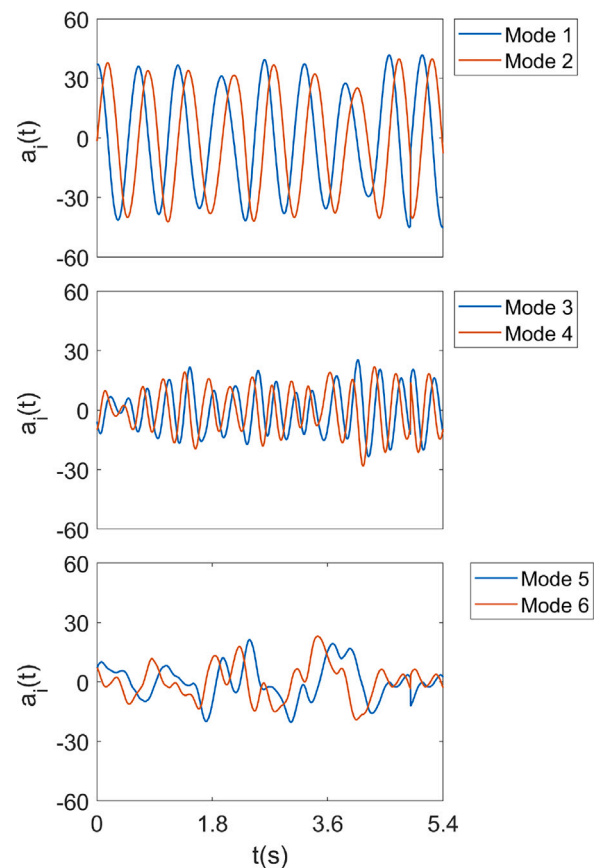Data will be made available on request.

Acknowledgement

Fig. B.22. Temporal coefficients of the first six POD modes obtained for the case with Fr = 0.40.

Appendix A. Contours of normalised vorticity behind the cylinder for the cases: Fr = 0.26, 0.40 and 0.45

The instantaneous flow generated behind the horizontal cylinder at four instants in time covering one vortex shedding cycle for the cases at Fr = 0.26, 0.40 and 0.45 are shown in Figs. A.19, A.20, and A.21 respectively. At Fr = 0.26, the von-Karman vortices are able to preserve their coherence because the free surface is located sufficiently above the cylinder to prevent any relevant free-surface effect. The von-Karman vortices lose their coherence more quickly at higher Fr whilst increasing the small-scale turbulence near the air–water interface due to interactions between the cylinder's vortical structures and the free-surface layer.

Appendix B. Temporal coefficients and power spectral density from the first six POD modes for the case Fr = 0.40

At Fr = 0.40, Fig. B.22 shows the time variation of the POD temporal coefficients corresponding to each of the first six modes shown in 9. The temporal coefficients for the first two modes fluctuate sinusoidally, resembling natural von-Karman vortex shedding. Moreover, the first pair's temporal coefficients exhibit a higher magnitude than the other pairs due to their higher energy contribution and coherence. Fig. B.23 shows the Power Spectral Density (PSD) distributions corresponding to the POD coefficients of the first six modes at Fr = 0.40, which can be employed to further determine the relationship between the POD eigenmodes and flow structures. The black dotted lines correspond to reference Strouhal numbers ($St = f_p D/U_0$) of 0.32 and its first harmonic ($2St$).
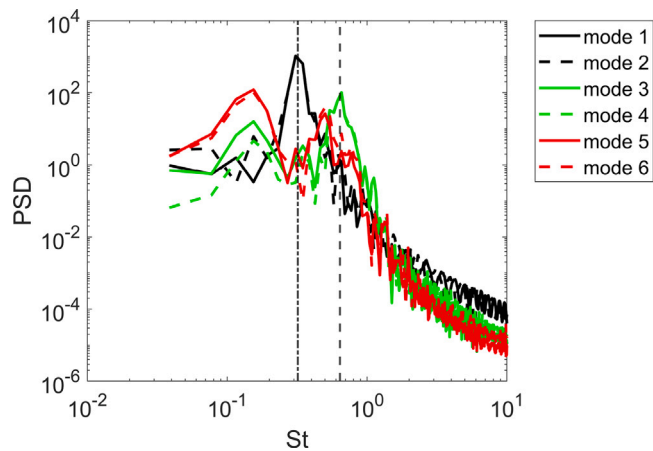
Fig. B.23. Power spectral density (PSD) of the temporal coefficients from the first six POD modes obtained for the case with $Fr = 0.40$. The dot-dashed line indicates the Strouhal number (St) frequency associated to the periodic vortex shedding and the dashed line indicates its first harmonic ($2St$).

References

[1] Müller S, Wilson CA, Ouro P, Cable J. Experimental investigation of physical leaky barrier design implications on juvenile rainbow trout (Oncorhynchus mykiss) movement. Water Resour Res 2021;57:1–17.

[2] Gerrard JH. The mechanics of the formation region of vortices behind bluff bodies. J Fluid Mech 1966;25:401–13.

[3] Sumner D, Heseltine JL, Dansereau OJP. Wake structure of a finite circular cylinder of small aspect ratio. Exp Fluids 2004;37:720–30.

[4] Alper Oner A, Salih Kirgoz M, Sami Akoz M. Interaction of a current with a circular cylinder near a rigid bed. Ocean Eng 2008;35:1492–504.

[5] Reichl P, Hourigan K, Thompson MC. Flow past a cylinder close to a free surface. J Fluid Mech 2005;533:269–96.

[6] Ouro P, Muhawenimana V, Wilson CA. Asymmetric wake of a horizontal cylinder in close proximity to a solid boundary for Reynolds numbers in the subcritical turbulence regime. Phys Rev Fluids 2019;4:1–28.

[7] Berger E, Wille R. Periodic flow phenomena. Annu Rev Fluid Mech 1972;4:313–40.

[8] Williamson CH. Vortex dynamics in the cylinder wake. Annu Rev Fluid Mech 1996;28:477–539.

[9] Sheridan J, Lin J-C, Rockwell D. Flow past a cylinder close to a free surface. J Fluid Mech 1997;330:1–30.

[10] Kahraman A, Ozgoren M, Sahin B. Flow structure from a horizontal cylinder coincident with a free surface in shallow water flow. Therm Sci 2012;16:93–107.

[11] Bouscasse B, Colagrossi A, Marrone S, Souto-Iglesias A. SPH modelling of viscous flow past a circular cylinder interacting with a free surface. Comput & Fluids 2017;146:190–212.

[12] Moballa B, Chern MJ, Borthwick AG. Incompressible SPH simulation of flow past horizontal cylinder between plane wall and free surface. J Fluids Struct 2020;97:103091.

[13] Zhao F, Wang R, Zhu H, Ping H, Bao Y, Zhou D, et al. Large-eddy simulations of flow past a circular cylinder near a free surface. Phys Fluids 2021;33:115108.

[14] Taira K, Brunton SL, Dawson ST, Rowley CW, Colonius T, McKeon BJ, et al. Modal analysis of fluid flows: An overview. AIAA J 2017;55:4013–41.

[15] Kevlahan NK, Hunt JC, Vassilicos JC. A comparison of different analytical techniques for identifying structures in turbulence. Appl Sci Res 1994;53:339–55.

[16] Ma X, Karniadakis GE. A low-dimensional model for simulating three-dimensional cylinder flow. J Fluid Mech 2002;458:181–90.

[17] Kostas J, Soria J, Chong MS. A comparison between snapshot POD analysis of PIV velocity and vorticity data. Exp Fluids 2005;38:146–60.

[18] Rehimi F, Aloui F, Nasrallah SB, Doubliez L, Legrand J. Experimental investigation of a confined flow downstream of a circular cylinder centred between two parallel walls. J Fluids Struct 2008;24:855–82.

[19] Sen U, Mukhopadhyay A, Sen S. Effects of fluid injection on dynamics of flow past a circular cylinder. Eur J Mech, B/Fluids 2017;61:187–99.

[20] Wang HF, Cao HL, Zhou Y. POD analysis of a finite-length cylinder near wake. Exp Fluids 2014;55:313–40.

[21] Mishra A, De A. Suppression of vortex shedding using a slit through the circular cylinder at low Reynolds number. Eur J Mech, B/Fluids 2021;89:349–66.

[22] Stoesser T, Braun C, Garcia-Villalba M, Rodi W. Turbulence structures in flow over two-dimensional dunes. J Hydraul Eng 2008;134:42–55.

[23] Ouro P, Lopez-Novoa U, Guest MF. On the performance of a highly-scalable computational fluid dynamics code on AMD, ARM and Intel processor-based HPC systems. Comput Phys Comm 2021;269:108105.

[24] Ouro P, Nishino T. Performance and wake characteristics of tidal turbines in an infinitely large array. J Fluid Mech 2021;925:1–32.

[25] Kara S, Kara MC, Stoesser T, Sturm TW. Free-surface versus rigid-Lid LES computations for bridge-abutment flow. J Hydraul Eng 2015;141:04015019.

[26] Christou A, Xie Z, Stoesser T, Ouro P. Propagation of a solitary wave over a finite submerged thin plate. Appl Ocean Res 2021;106:102425.

[27] McSherry R, Chua K, Stoesser T, Mulahasan S. Free surface flow over square bars at intermediate relative submergence. J Hydraul Res 2018;56:825–43.

[28] Jalalabadi R, Stoesser T, Ouro P, Luo Q, Xie Z. Free surface flow over square bars at different Reynolds numbers. J Hydro-Environ Res 2021;36:67–76.

[29] Liu Y, Stoesser T, Fang H. Effect of secondary currents on the flow and turbulence in partially filled pipes. J Fluid Mech 2022;938:A16.

[30] Bomminayuni S, Stoesser T. Turbulence statistics in an open-channel flow over a rough bed. J Hydraul Eng 2011;137:1347–58.

[31] Nikora VI, Stoesser T, Cameron SM, Stewart M, Papadopoulos K, Ouro P, et al. Friction factor decomposition for rough-wall flows: Theoretical background and application to open-channel flows. J Fluid Mech 2019;872:626–64.

[32] Liu Y, Stoesser T, Fang H, Papanicolaou A, Tsakiris AG. Turbulent flow over an array of boulders placed on a rough, permeable bed. Comput & Fluids 2017;158:120–32.

[33] Stoesser T. Large-eddy simulation in hydraulics: Quo Vadis? J Hydraul Res 2014;52:441–52.

[34] Nicoud F, Ducros F. Subgrid-scale stress modelling based on the square of the velocity. Flow Meas Instrum 1999;62:183–200.

[35] Uhlmann M. An immersed boundary method with direct forcing for the simulation of particulate flows. J Comput Phys 2005;209:448–76.

[36] Osher S, Sethian JA. Fronts propagating with curvature-dependent speed: Algorithms based on Hamilton-Jacobi formulations. J Comput Phys 1988;79:12–49.

[37] Sussman M. A level set approach for computing solutions to incompressible two-phase flow. J Comput Phys 1994;114:146–59.

[38] Kang S, Sotiropoulos F. Large-eddy simulation of three-dimensional turbulent free surface flow past a complex stream restoration structure. J Hydraul Eng 2015;141:04015022.

[39] Yokoi K, Onishi R, Deng XL, Sussman M. Density-scaled balanced continuum surface force model with a level set based curvature interpolation technique. Int J Comput Methods 2016;13:1–20.

[40] Muhawenimana V, Wilson CA, Ouro P, Cable J. Spanwise cylinder wake hydrodynamics and fish behavior. Water Resour Res 2019;55:8569–82.

[41] Lumley JL. The structure of inhomogeneous turbulent flows. Atmos Turbul Radio Wave Propag 1967;166–78.

[42] Chatterjee A. An introduction to the proper orthogonal decomposition. Current Sci 2000;78:808–17.

[43] Holmes P, Lumley JL, Berkooz G. Turbulence, coherent structures, dynamical systems and symmetry. New York: Cambridge University Press; 1996.

[44] Sirovich L. Turbulence and the dynamics of coherent structures. III. Dynamics and scaling. Quart Appl Math 1987;45:583–90.

[45] Tang SL, Djenidi L, Antonia RA, Zhou Y. Comparison between velocity- and vorticity-based POD methods in a turbulent wake. Exp Fluids 2015;56:1–12.

[46] Aljure DE, Lehmkhul O, Rodríguez I, Oliva A. Three dimensionality in the wake of the flow around a circular cylinder at Reynolds number 5000. Comput & Fluids 2017;147:102–18.

[47] Dipankar A, Sengupta TK, Talla SB. Suppression of vortex shedding behind a circular cylinder by another control cylinder at low Reynolds numbers. J Fluid Mech 2007;573:171–90.

[48] Perrin R, Braza M, Cid E, Cazin S, Barthet A, Sevrain A, et al. Obtaining phase averaged turbulence properties in the near wake of a circular cylinder at high Reynolds number using POD. Exp Fluids 2007;43:341–55.

[49] Vitkovicova R, Yokoi Y, Hyhlik T. Identification of structures and mechanisms in a flow field by POD analysis for input data obtained from visualization and PIV. Exp Fluids 2020;61:1–21.

[50] Ribau ÂM, Gonçalves ND, Ferrás LL, Afonso AM. Flow structures identification through proper orthogonal decomposition : The flow around two distinct cylinders. Fluids 2021;6:1–20.

[51] Deep D, Sahasranaman A, Senthilkumar S. POD analysis of the wake behind a circular cylinder with splitter plate. Eur J Mech B/Fluids 2022;93:1–12.

[52] Yang X, Foti D, Kelley C, Maniaci D, Sotiropoulos F. Wake statistics of different-scalewind turbines under turbulent boundary layer inflow. Energies 2020;13:1–17.

[53] Papaioannou GV, Yue DK, Triantafyllou MS, Karniadakis GE. Evidence of holes in the arnold tongues of flow past two oscillating cylinders. Phys Rev Lett 2006;96:1–4.

[54] Zhang M, Zheng ZC. Relations of POD modes and Lyapunov exponents to the nonlinear dynamic states in flow over oscillating tandem cylinders. Phys Fluids 2018;123602:1–17.

[55] Xia C, Wei Z, Yuan H, Li Q, Yang Z. POD analysis of the wake behind a circular cylinder coated with porous media. J Vis 2018;21:965–85.

[56] Berkooz G, Holmes P, Lumley JL. The proper orthogonal, decomposition in the analysis of turbulent flows. Ann Rev Fluid Mech 1993;25:539–75.

[57] Kuzmina K, Marchevsky I, Soldatova I, Izmailova Y. On the scope of lagrangian vortex methods for two-dimensional flow simulations and the POD technique application for data storing and analyzing. Entropy 2021;23:1–39.

[58] Stoesser T, Kim S, Diplas P. Turbulent flow through idealized emergent vegetation. J Hydraul Eng 2010;136(12):1003–17.

[59] Rubinstein R, Clark TT. "Equilibrium" and "non-equilibrium" turbulence. Theor Appl Mech Lett 2017;7(5):301–5.

[60] Zhao F, Wang R, Zhu H, Ping H, Bao Y, Zhou D, et al. Large-eddy simulations of flow past a circular cylinder near a free surface. Phys Fluids 2021;33(11):115108.